Biophysical Journal
Article

Biophysical Society

Prospects for Human Erythrocyte Skeleton-Bilayer Dissociation during Splenic Flow

Qiang Zhu,[1] Sara Salehyar,[1] Pedro Cabrales,[1] and Robert J. Asaro[1,*]
[1]Department of Structural Engineering, University of California, San Diego, La Jolla, California

ABSTRACT Prospects of vesiculation occurring during splenic flow of erythrocytes are addressed via model simulations of RBC flow through the venous slits of the human spleen. Our model is multiscale and contains a thermally activated rate-dependent description of the entropic elasticity of the RBC spectrin cytoskeleton, including domain unfolding/refolding. Our model also includes detail of the skeleton attachment to the fluidlike lipid bilayer membrane, including a specific accounting for the expansion/contraction of the skeleton that may occur via anchor protein diffusive motion, that is, band 3 and glycophorin, through the membrane. This ability allows us to follow the change in anchor density and thereby the strength of the skeleton/membrane attachment. We define a negative pressure between the skeleton/membrane connection that promotes separation; critical levels for this are estimated using published data on the work of adhesion of this connection. By following the maximum range of negative pressure, along with the observed slight decrease in skeletal density, we conclude that there must be biochemical influences that probably include binding of degraded hemoglobin, among other things, that significantly reduce effective attachment density. These findings are consistent with reported trends in vesiculation that are believed to occur in cases of various hereditary anemias and during blood storage. Our findings also suggest pathways for further study of erythrocyte vesiculation that point to the criticality of understanding the biochemical phenomena involved with cytoskeleton/membrane attachment.

INTRODUCTION

The spleen uses, in concert, both innate and adaptive mechanisms to provide a unique immune and filtering system for the blood (1). Of direct interest here is its ability to remove older or defective erythrocytes from circulation. Moreover, the action of the spleen may also be to produce vesicles containing removal molecules (i.e., those damaged such as denatured hemoglobin) as a self-protective mechanism (2), thereby guarding against premature cell removal. For example, one of the recognition mechanisms in the spleen involves Heinz bodies. They are intraerythrocytic inclusions of hemichrome formed from the oxidized or denatured hemoglobin typically found in aged red cells. They have also been found in drug-induced hemolytic anemia, resulting from defects in the red blood cell (RBC) reducing system (e.g., glucose 6-phosphate dehydrogenase deficiency) (3,4). The rigid intraerythrocytic hemichrome inclusions are known to act as sticking points, causing Heinz body-containing erythrocytes to be trapped (5). Thus, there are other causes of erythrocyte vesiculation not related to splenic flow as noted below in the Discussion, where the notions of nano- and microvesiculation are defined and discussed.

The specialized structure of the venous system gives the spleen the ability to sequester erythrocytes in an environment containing macrophages (1,6). Most important here are the venous sinus slits through which erythrocytes flow as schematized in Fig. 1. The sinuses are lined by endothelial cells and possess stress fibers running parallel to the cellular axis (again see Fig. 1 and its *insets*). The stress fibers are composed of actin- and myosinlike filaments suggesting that they act in a slidinglike action that, in turn, controls the caliber (the spacing of the slits). Indeed, MacDonald et al. (7) performed a remarkable series of experiments involving in vivo microscopy of RBC flow through rat sinus slits that demonstrated that the slit caliber varies in time. In observing given slits, they reported that slits are open (i.e., they allow RBC passage) for only ~19% of the times they were observed. Chen and Weiss (8) reported that their observed slit caliber in rats ranged from 0.2 to 0.5 μm; for perspective the rat RBC diameter is of order 6.5 μm as compared to human RBC diameters on order of 8.5 μm. The reported slit size for human is ~1 μm (9). We will assume herein that the operative slit caliber of human sinus slits is in the range $0.6\ \mu\text{m} \leq \delta \leq 1.5\ \mu\text{m}$.

Submitted August 12, 2016, and accepted for publication May 23, 2017.
*Correspondence: rasaro@san.rr.com
Editor: Markus Deserno.
http://dx.doi.org/10.1016/j.bpj.2017.05.052

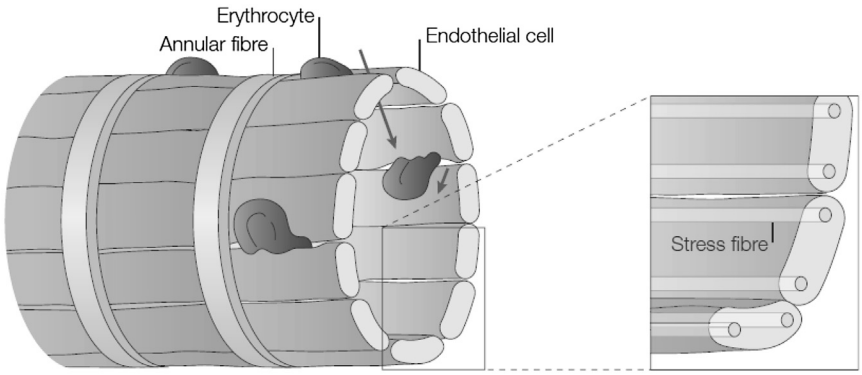

FIGURE 1 Sinus slits of the spleen. The drawing is taken from Mebius and Kraal (1).

With aging, erythrocytes experience degradation of membrane and cell components (for example, hemoglobin proteolysis and band 3/glycophorin degradation (10,11)). To prevent premature cell elimination, such degraded components are shed within vesicles formed during flow through the spleen (2,11,12). As this occurs, cell volume and cell hemoglobin content decrease by as much as 30 and 20%, respectively. Subsequently, hemoglobin concentration increases by ~14%. Indeed, it is reported that the hemoglobin concentration within spleen-shed vesicles is quite similar to that found in older cells as measured by their HbA1c concentrations. Vesicles shed this way are deficient in spectrin but contain band 3 and glycophorin (13–15). Because the cytosol viscosity is known to increase nonlinearly with hemoglobin concentration, it is also suspected that this may impede cell passage through the venous slits and limit cell life (16,17). It is, however, interesting that we reveal herein that the probability of splenic vesiculation tends to decrease with increasing cytosol viscosity. This is, to our knowledge, a novel observation made via the results we present below. To understand these effects, a comprehensive numerical model is needed to predict large deformation and vesiculation rate of erythrocyte as a function of the initial volume, mechanical strain, cell adhesion, and geometry. This model will provide a rigorous yet flexible platform for developing multiphysics models at any scale of interest.

Based on the above observations, Bosman et al. (11) have proposed that erythrocyte vesiculation is a key mechanism of cell aging. Accordingly, we have explored the process of possible vesiculation during splenic flow via simulation to determine mechanisms of forming vesicles and the detailed conditions required for vesiculation to occur. Indeed, we find that to cause vesiculation it is necessary for the density of anchorages (i.e., integral membrane proteins such as band 3 and glycophorin) of the erythrocyte spectrin skeleton to the bilipid membrane be reduced to values $<10\%$ of their nominal values. However, whereas such reductions in skeletal density occurs during ex vivo processes, such as erythrocyte flow through narrow pipettes (18), there is not enough time for such large reductions to occur during splenic flow. Thus, we conclude that other causes of anchorage density decrease must occur—these would include binding of hemoglobin as suggested by Bosman et al. (11).

This view is consistent with observations of increased vesiculation in the presence of membranopathies and/or hemoglobinopathies (19). In hereditary spherocytosis, characterized by deficiencies in membrane or cytoskeleton proteins, such as in ankyrin, band 3, 4.2, or α,β spectrin (20), the skeleton/membrane anchorages are clearly reduced. Similarly in hereditary elliptocytosis, characterized by lateral defects in the α,β spectrin linkage and in protein 4.1, skeleton integrity and its attachment to the membrane are compromised. In cases of hereditary hemoglobinopathies, unstable hemoglobin induces oxidation of membrane lipids and binding of hemoglobin to the membrane (21) that likewise reduce skeleton/membrane anchorage. In fact, microvesicles obtained from stored blood are found devoid of cytoskeleton proteins but to contain actin and band 3 in aggregated or degraded form (22–25). This is discussed further after our simulation results are reviewed.

The plan of the article and the steps involved are as follows: our simulations describe the flow of RBCs through the venous slits of the spleen to explore the possible conditions that may cause, or allow, vesiculation. Thereby we first describe a computational configuration to simulate the process of a RBC being driven through a slit, to mimic the venous slits, driven by a pressure difference. The simulation model and methods are then described along with results. In presenting results we focus on describing the maximum dissociation stress between the cytoskeleton and the lipid bilayer, because this tends to separate the membrane from the skeleton. Sufficiently high stress may trigger the separation of the skeleton from the bilipid membrane and vesiculation. We also focus on the transit time of a RBC through a slit, because this is important for determining if sufficient time is available for skeleton restructuring via anchoring protein motion (i.e. diffusion) within the membrane. To

quantitatively interpret the results, we then explore the strength of the skeleton/membrane connection by analysis of existing data concerning the work of adhesion of that interface and also existing molecular theory concerning bond strength. Of particular interest are: 1) the mechanisms by which vesicles form during splenic flow; 2) the conditions, vis-à-vis the density of anchorages required for vesiculation to occur; and 3) the separation stresses that can develop to cause vesiculation. Summary and conclusions follow.

MATERIALS AND METHODS

Problem description

As demonstrated in Fig. 2, we consider the translocation process of a red blood cell through a slit located in the middle of a rectangular channel. The dimensions of the channel are 64 (in x direction), 20 (in y direction), and 20 μm (in z direction). The slit has well-rounded edges. Its depth (in x direction) is fixed to be 2 μm, whereas the width δ (in y direction) can be varied.

As noted above, we take the slit caliber in any given simulation to be constant, and in the range $0.6\ \mu m \leq \delta \leq 1.5\ \mu m$. It is worthwhile to note, however, that our model is fully capable of simulating time-variable calibers as observed in the experiments of MacDonald et al. (7). This could well be critical for accounting for the total throughput of RBCs and for the time's history of vesiculation that occurs within splenic flow.

Unlike recent studies of RBC passing through a slit after an incoming flow (26,27), in this investigation the motion of the cell is driven by a pressure difference—the pressure at the inlet is prescribed to be P and the pressure at the outlet is 0. Motivation for this change to imposed pressure differences comes from at least two directions: 1) the computational cost and the necessity to study cases with viscosity ratios other than one, and 2) the convenience to relate this configuration with experimental setups (e.g., (28)). To elaborate, we note that in a flow-driven configuration it is necessary to employ a doubly periodic condition in the lateral directions. With such a condition instead of two blocks to form the slit, there is an infinite number of them (otherwise the cell will just go around the blocks without passing through the slit). Although there exist efficient algorithms, the computational effort is still formidable, considering the large number of elements we use. This makes it computationally infeasible to study viscosity ratios other than 1 because it involves an iteration scheme for fluid-cell interaction at each time step. For this reason, in the previous work we concentrated on the viscosity ratio of 1, which is not physiologically relevant (27). On the other hand, in this study we create a closed computational domain to avoid the doubly periodic conditions. Mathematically, such a configuration requires knowledge of the pressure at the inlet and outlet so that it leads to a pressure-driven process. Moreover, the pressure-driven configuration we use in this study is similar to experimental settings so that it will be more natural and accurate to relate our results with experimental observations.

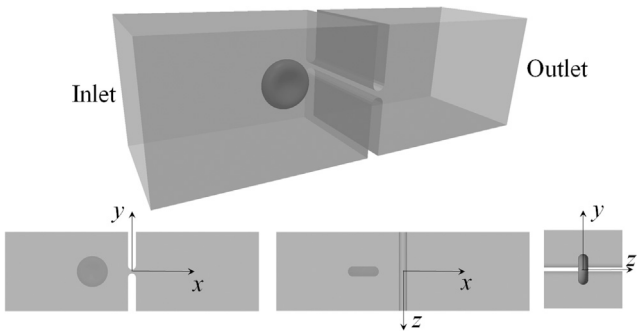

FIGURE 2 Translocation of RBC through a slit in a rectangular channel.

The mechanical properties of the cell membrane, including the lipid bilayer and the cytoskeleton, are listed in Tables 1 and 2. The viscosity of the fluid inside the cell (i.e., cytosol) is 0.006 pN s μm^{-2} (29). The normal viscosity of blood plasma, on the other hand, ranges between 0.011 and 0.013 pN s μm^{-2} (30). Therefore it is reasonable to assume that a physiologically relevant value of viscosity ratio Λ (the ratio between the viscosity of the surrounding fluid and that of the cytosol) is 5 (16,26,31).

Mathematical formulation and numerical model

The problem shown in Fig. 2 is studied numerically by coupling a multiscale structural model of the red blood cell with a Stokes-flow-based boundary-element model that solves the flow fields inside and outside of the cell simultaneously. In the following, we briefly describe the primary characteristics of these models. The details are included in our previous publications (18,32–34).

Multiscale model of RBCs

Unlike most existing models of erythrocytes, which simplify the membrane as a single layer of elastic or viscoelastic material with uniform properties, in our description we model this biological structure as two layers with distinctive material properties using a finite-element approach (18). The outer layer represents the lipid bilayer. It has large area stiffness, finite bending stiffness, and tiny shear stiffness (referring to the fact that this material is fluidlike). The inner layer represents the cytoskeleton. It has finite area and shear stiffness but tiny bending stiffness. Due to the mobility of the pinning points (band 3 and glycophorin C) between them, the two layers can slide against each other. This fact is incorporated into our model by depicting the interaction between the two layers as a viscous friction in the tangential (in-plane) direction (following the derivation in our previous work, the friction coefficient is chosen to be 144 ρ/ρ_0 pN s μm^{-3}, where ρ and ρ_0 are the deformed and initial protein densities of the cytoskeleton, respectively (34)). This characteristic allows us to study scenarios in which the inner and outer layers develop different local (area or shear) deformations during dynamic processes (35). Moreover, the double-layer representation allows us to predict the contact stress between the cytoskeleton and the lipid bilayer, which is critical for this study. In this model the connectivity between the outer layer (lipid bilayer) and the inner layer (skeleton) is depicted by distributions of linear springs. The stress inside these springs represents the contact stress between the layers. The fracture of these springs when the stress exceeds the limiting value allows simulation of skeleton-bilayer dissociation (18).

The mechanical properties of the lipid bilayer (e.g. the bending stiffness) are taken from reported values in the literature (see Table 1). The properties of the cytoskeleton (specifically, its area and shear stiffness) are obtained from a mesoscale model of the 3D molecular architecture of a junctional complex (JC), the basic unit in the cytoskeleton (33). The JC contains a central piece of actin protofilament (modeled as a rigid rod) surrounded by six flexible spectrin dimers (Sp), modeled as nonlinear springs, as described in the following paragraph. In our model, the exact configuration of this structure is based on state-of-the-art understanding of its molecular structure.

TABLE 1 Parameters of the Lipid Bilayer

h_b (nm)	μ_b (pN μm^{-1})	K_b (pN μm^{-1})	k_c (J)	ν_b (pN s μm^{-1})
2.2	10^{-3}	9.6×10^2	2×10^{-19}	10^{-3}

h_b, bilayer thickness (different from reality due to the homogeneous shell assumption); μ_b, bilayer shear stiffness (a very small value to stabilize numerical algorithm); K_b, bilayer areal stiffness; k_c, bilayer bending stiffness (42); ν_b, bilayer viscosity (63).

TABLE 2 Parameters of the Cytoskeleton

h_s (nm)	ν_s (pN s μm^{-1})	p_f (nm)	p_u (nm)	L_f (nm)
2	0.0625	11.12	0.8	6.39
L_u (nm)	$\Delta\Delta x^*$ (nm)	$F_{1/2}$ (pN)	μ_s (pN μm^{-1})	
39	12.6	12	5.7	

h_s, cytoskeleton thickness; ν_s, cytoskeleton viscosity (64); p_f, persistence length of folded domains in Sp; p_u, persistence length of unfolded domains (32); L_f, contour length of folded domains (32); L_u, contour length of unfolded domains (32); $\Delta\Delta x^*$, the difference between the activation length of the unfolding process and that of the refolding process (32); $F_{1/2}$, the force corresponding to the state when half of the domains are unfolded (32); μ_s, initial shear modulus of the cytoskeleton (65). A spectrin consists of 19 domains in our model.

This model predicts the area and shear stiffness of the cytoskeleton as nonlinear functions of its local deformation (rather than constants used in other models) so they vary both spatially and temporally. These properties are then used by the double-layer membrane model in the complete-cell level.

Conventionally, spectrin dimers are modeled as nonlinear springs with wormlike-chain behavior. This simple depiction is consistent with the tension-elongation curve of Sp in relatively small deformations. In large deformations, however, the wormlike-chain model is incapable of reproducing the domain-unfolding effects (i.e., when overstretched the folded domains in Sp may open and release internal tension). With domain unfolding modeled as a thermally activated process, this issue has been fixed in our Sp model (32). The Sp model is embedded into the mesoscale JC model for high-fidelity prediction of the mechanical properties of the cytoskeleton in arbitrary deformations.

Fluid-cell interactions

Within the low-Reynolds number regime, at any point $\mathbf{x}_0$ on the cell surface, the velocity $\mathbf{v}$ satisfies the following boundary integral equation:

$$\begin{aligned}\mathbf{v}(\mathbf{x}_0) = &-\frac{1}{4\pi\eta_1(1+\Lambda)}\left[\iint_{\Gamma_c}\mathbf{G}(\mathbf{x},\mathbf{x}_0)\cdot\Delta\mathbf{f}(\mathbf{x})d\Gamma(\mathbf{x})\right.\\&+\iint_{\Gamma_b}\mathbf{G}(\mathbf{x},\mathbf{x}_0)\cdot\mathbf{f}(\mathbf{x})d\Gamma(\mathbf{x})\\&\left.-P\iint_{\Gamma_i}\mathbf{G}(\mathbf{x},\mathbf{x}_0)\cdot\hat{\mathbf{x}}d\Gamma(\mathbf{x})\right]\\&+\frac{1-\Lambda}{4\pi(1+\Lambda)}-\iint_{\Gamma_c}\mathbf{v}(\mathbf{x})\cdot\mathbf{T}(\mathbf{x},\mathbf{x}_0)\cdot\mathbf{n}(\mathbf{x})d\Gamma(\mathbf{x})\\&+\frac{1}{4\pi(1+\Lambda)}\iint_{\Gamma_i+\Gamma_o}\mathbf{v}(\mathbf{x})\cdot\mathbf{T}(\mathbf{x},\mathbf{x}_0)\cdot\mathbf{n}(\mathbf{x})d\Gamma(\mathbf{x}),\end{aligned}\tag{1}$$

where Γ_c is the fluid-cell boundary, Γ_b is the surface of the solid boundary, Γ_i is the inlet, and Γ_o is the outlet; η_1 is the viscosity of the external fluid; Λ is the viscosity ratio ($\Lambda = \eta_2/\eta_1$, where η_2 is the viscosity of the internal fluid); the vector $\Delta\mathbf{f}$ is the total traction (the difference between the tractions outside and inside the cell) on the cell membrane; the vector $\mathbf{f}$ is the traction on the solid boundary; $-\int\int$ denotes the principal value integration; the vector $\hat{\mathbf{x}}$ is a unit vector in the x direction; and $\mathbf{n}$ is a unit normal vector pointing out of the cell. The matrix $\mathbf{G}$ contains the Green's function for velocity G_{ij}, given as

$$G_{ij}(\mathbf{x},\mathbf{x}_0) = \frac{\delta_{ij}}{|\mathbf{x}-\mathbf{x}_0|}+\frac{(x_i-x_{0_i})(x_j-x_{0_j})}{|\mathbf{x}-\mathbf{x}_0|^3},\tag{2}$$

where δ_{ij} is Kronecker's delta, and the matrix $\mathbf{T}$ is the Green's function for stress. Its components T_{ijk} are

$$T_{ijk}(\mathbf{x},\mathbf{x}_0) = -6\frac{(x_i-x_{0_i})(x_j-x_{0_j})(x_k-x_{0_k})}{|\mathbf{x}-\mathbf{x}_0|^5}.\tag{3}$$

On the boundaries (Γ_b, Γ_i, or Γ_o), we have

$$\begin{aligned}\mathbf{v}(\mathbf{x}_0) = &-\frac{1}{4\pi\eta_1}\left[\iint_{\Gamma_c}\mathbf{G}(\mathbf{x},\mathbf{x}_0)\cdot\Delta\mathbf{f}(\mathbf{x})d\Gamma(\mathbf{x})\right.\\&+\iint_{\Gamma_b}\mathbf{G}(\mathbf{x},\mathbf{x}_0)\cdot\mathbf{f}(\mathbf{x})d\Gamma(\mathbf{x})\\&\left.-P\iint_{\Gamma_i}\mathbf{G}(\mathbf{x},\mathbf{x}_0)\cdot\hat{\mathbf{x}}d\Gamma(\mathbf{x})\right]\\&+\frac{1-\Lambda}{4\pi}\iint_{\Gamma_c}\mathbf{v}(\mathbf{x})\cdot\mathbf{T}(\mathbf{x},\mathbf{x}_0)\cdot\mathbf{n}(\mathbf{x})d\Gamma(\mathbf{x})\\&+\frac{1}{4\pi}-\iint_{\Gamma_i+\Gamma_o}\mathbf{v}(\mathbf{x})\cdot\mathbf{T}(\mathbf{x},\mathbf{x}_0)\cdot\mathbf{n}(\mathbf{x})d\Gamma(\mathbf{x}),\end{aligned}\tag{4}$$

where $\mathbf{v}(\mathbf{x}_0) = 0$ on the solid boundary due to the no-slip, no-flux condition.

By using a boundary-element approach, Eqs. 1 and 4 are solved together iteratively to find the updated velocity of the cell. A forward Newtonian integration algorithm is then employed to update the new location of each collocation point on the cell surface. To prevent the singularity that arises when the cell membrane approaches too close to the solid boundary, a repulsive zone with a thickness of 100 nm is introduced between the cell and slit surface. Whenever the cell membrane enters this zone, it is repelled by a pressure along the normal direction of the boundary. The physical basis of this zone is the layer of endothelial glycocalyx consisting of glycoproteins and other molecules that covers the endothelial cells (36,37). In addition, electrostatic forces exist that repel the cell from the endothelial cells of the slits. This is explored below.

Perspective on glycocalyx repulsive forces

The glycocalyx is an extracellular layer that consists of glycolipids and glycoproteins that protrude from the bilipid membrane surface (38–40). It is, in essence, a polyelectrolyte anchored to an electrically neutral membrane. Sialylated glycoproteins within it induce a negative charge that creates an negative surface potential, ψ_s; this, in turn creates a repulsive force between cells each possessing such a potential. The thickness of the glycocalyx is thought to be in the range 5–10 nm (38,39).

As the cell is in an ionic environment, an electrical double layer forms, as described by the Gouy-Chapman analysis (41). When two such layers overlap, the equilibrium charge and potential fields are perturbed and a repulsive force, or stress σ_e, between the cells' surfaces develops. Such stresses have been analyzed (e.g., (41)) and for this case, where we assume that the surface potential is the same for each cell, they take the form

$$\sigma_e = \frac{\epsilon\kappa_D^2\psi_s^2}{[\cosh(\kappa h)+1]},\tag{5}$$

where E is the medium's dielectric permittivity with units [$C^2/(Nm^2)$]; κ_D is the inverse Debye length with units [m^{-1}]; ψ_s is the surface potential with units [V]; and h is the separation between the charged layers in units of [m].

To explore magnitudes, we will take $\psi_s = -15$ mV, $\kappa_D = 10^9\ m^{-1}$, which is appropriate for a medium with an ionic concentration in the range 0.1–0.15 M (41), $E = 6.96 \times 10^{-10}$, and $h \sim 10$–15 nm. This yields

$$\sigma_e \approx 14\ \text{Pa if } h = 10\ \text{nm}, \quad \approx 0.1\ \text{Pa if } h = 15\ \text{nm}. \tag{6}$$

The scenario this numerology depicts is this: an erythrocyte with a surface potential in the range $-20\ \text{mV} \le \psi_s \le -10$ mV may approach a surface of similar potential up to a distance of, say, 15 nm. At that distance, the repulsive electrostatic stress rises exponentially, as described by Eq. 5. As the glycocalyx itself has a thickness in the range $5\ \text{nm} \le h_g \le 10$ nm, where steric repulsion would set in, the repulsive stress would rise even more dramatically. Thus we expect that at separations of, say, $h = 15 + 2(10) = 35$ nm, an essentially rigid standoff is reached. To date, we have used a standoff of 100 nm; we continue to use this value because, whereas it aids in numerical stability, it contributes little or no inaccuracy by the above perspective. Even if surface potentials were on the order of $\psi_s \sim -30$ mV, this would change the picture little.

On the other hand, the effects of electrostatic interactions remain to be explored with regard to interactions among smaller structures such as vesicles of dimensions of order 200–400 nm. This topic will drive future research.

RESULTS

In the following simulations, we consider two different initial orientations of the cell—Orientation 1 (Fig. 3) and Orientation 2 (Fig. 4). According to our previous studies (27), these two orientations lead to large cell deformations, and subsequently large contact stress between the skeleton and the lipid bilayer. Overall, we use 6000 elements on the cell membrane and 2500 elements on the solid boundary (with mesh density increased near the slit). We first concentrate on a slit width of 1 μm. Effects of slit size will be explored later.

Figs. 3 and 4 demonstrate snapshots of the cell during its passage through the slit with $\delta = 1$ μm and $P = 200$ Pa. In both cases, infolding (referring to the formation of a concave shape on the cell membrane, as shown in both figures at $t = 0.0145$ s) is observed in the later stage of the translocation before the cell leaves the slit. This is consistent with our previous simulations of a flow-driven translocation problem (27). There are, however, differences in the detailed cell deformations. In particular, we note that the occurrence of infolding in these cases is much less significant than the one observed in the previous study (see, e.g., Fig. 2 in (27)). In addition to differences in setup (pressure-driven translocation in a closed channel versus flow-driven translocation in a periodic computational domain), this is attributed to the difference in viscosity ratio Λ. In this study, the value of Λ is chosen to be 5, much larger than the one used in the previous simulations ($\Lambda = 1$), although consistent with conditions in vivo. Higher viscosity ratio greatly reduces the flexibility of a cell, leading to changes in cell deformation, especially the formation of infolding areas.

Fig. 5 *a* summarizes the transit time T (defined as the difference between the time when part of the membrane enters the slit and the time when the cell completely leaves the slit) at different values of the applied pressure difference P. It is seen that within the range of P considered in this research ($50\ \text{Pa} \le P \le 200$ Pa), the transit time varies between 0.012 and 0.053 s. The reported value of T based on the in vivo experiments is 0.02–64 s, with the peak occurring at ~0.1 s (7). This indicates that although the actual pressure drop in physiological conditions is not available, the range of P chosen in our simulations is physiologically relevant (we focus on the lower side of T because our simulations suggest that these cases are usually associated with large contact stress between the lipid bilayer and the cytoskeleton).

In Fig. 5 *b*, we plot the typical time histories of the maximum dissociation stress σ at P = 200 Pa. Hereby σ is defined as the biggest negative contact stress (the interaction

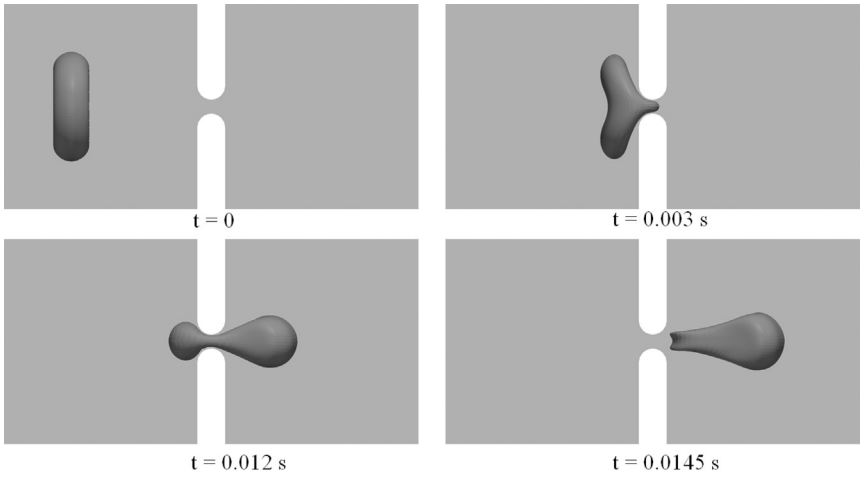

FIGURE 3 Snapshots of cell deformations as the cell passes through the slit at $P = 200$ Pa with Orientation 1. The width of the slit (δ) is 1 μm.

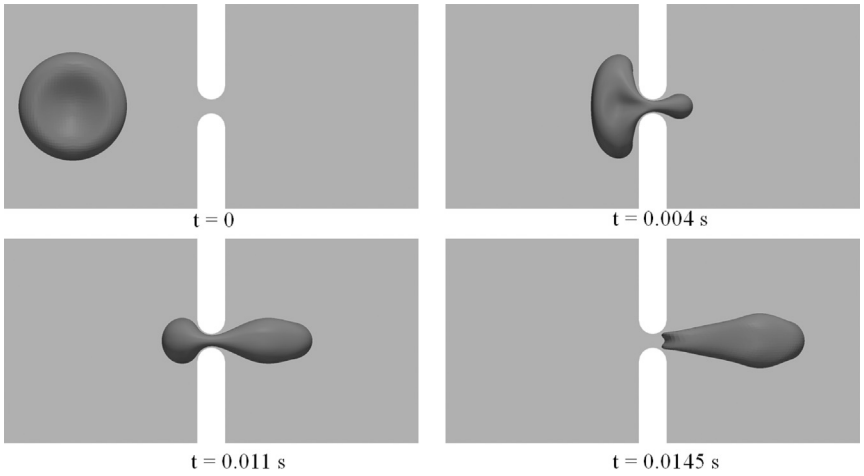

FIGURE 4 Snapshots of cell deformations as the cell passes through the slit at $P = 200$ Pa with Orientation 2. The width of the slit (δ) is 1 μm.

force between the skeleton and the bilayer in the normal direction per unit area) over the entire cell membrane at any instant. In our model, positive values of the contact stress refer to scenarios when the cytoskeleton and the lipid bilayer are pushed toward each other, whereas negative values refer to cases when they are pulled away from each other. It is seen that with both initial orientations, the peak values of σ (hereafter referred to as σ_p) occur at the late stage of translocation when the cell is about to leave the slit and recover its original biconcave configuration. The detailed distributions of the contact stress at one particular instant are shown in Fig. 6 *a* and *b*. Large dissociation stress is seen to be concentrated at the edges of the infolded area together with significant bending deformation. Indeed, it is in these regions that vesiculation is expected to occur.

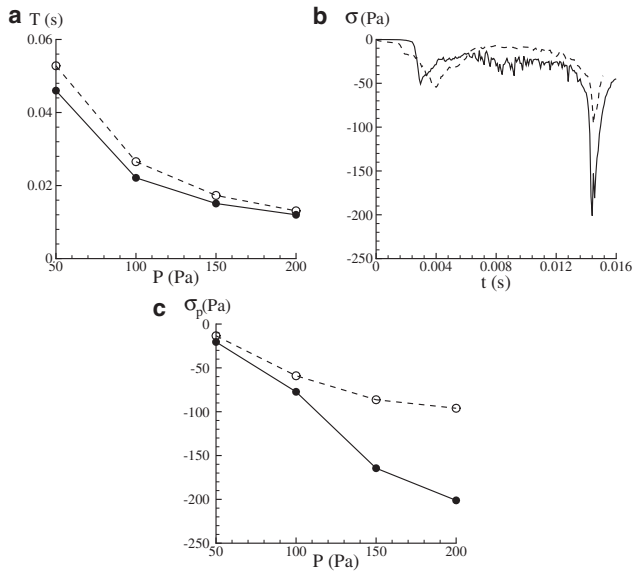

FIGURE 5 (*a*) Given here is the dependence of transit time T upon the pressure difference P. (*b*) Given here are variations of σ (the maximum dissociation stress) in time. (*c*) Given here are values of σ_p (peak values of the maximum dissociation contact stress) at different pressure difference measures of P. In all the plots, results from Orientation 1 are shown in solid lines, whereas those from Orientation 2 are shown in dashed lines. $\delta = 1$ μm.

In Fig. 6, *c* and *d*, we plot the corresponding area deformation of the cytoskeleton. Hereby the area deformation is defined as $\alpha = \lambda_1\lambda_2$, where λ_1 and λ_2 are the two principle in-plane stretches. The value α is related to the density change of the skeleton through $\rho/\rho_0 = 1/\alpha$; $\alpha > 1$ represents area expansion (associated with the decrease in the density of band 3 and glycophorin that connect the skeleton to the lipid), and $\alpha < 1$ represents area compression (with the increase in the density of the transmembrane proteins). Our results show that at the locations with significant dissociation stress, there is almost no change in skeleton density ($\alpha \sim 1$). The maximum area change elsewhere is ~5–6% (area compression), which is negligible in comparison with the area deformation in a typical micropipette aspiration (18). This is attributed to the small timescale of the translocation process—there is no sufficient time for significant sliding between the lipid bilayer and the skeleton. Moreover, as pointed out in our previous work (27), the small but finite area deformation shown in these simulation is actually caused by the reduced area stiffness of the lipid bilayer. For numerical stability, we have to use an area modulus of 9.6×10^2 pN μm^{-1}, rather than the measured value of 5×10^5 pN μm^{-1} (42). Subsequently our model tends to overestimate the area deformation. With this fact taken into account, we expect that the area deformation of the cytoskeleton is insignificant and its effect in the areal density of JC is negligible. In comparison, our previous simulations show that in a typical micropipette aspiration with a pipette radius of $R_p = 0.668$ μm, as the aspired length is $8R_p$ the skeleton area expansion factor α near the cap may reach 7 (or even higher with larger aspired length when spectrin unfolding occurs) (18). Similar large area deformation of the cytoskeleton

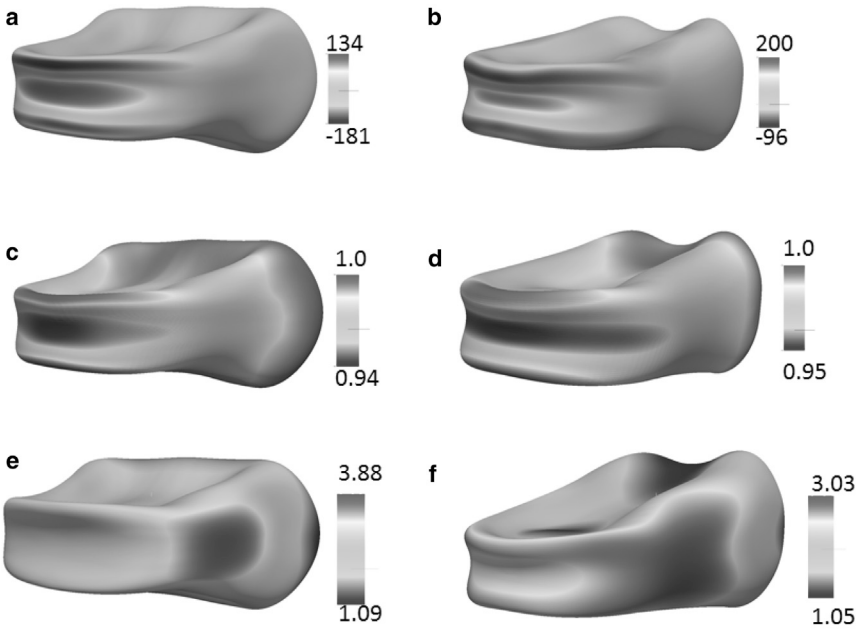

FIGURE 6 Distributions of the contact stress (*a* and *b*), area deformations (*c* and *d*), and shear deformations of the cytoskeleton (*e* and *f*). (*a*), (*c*), and (*e*) are from Orientation 1, whereas (*b*), (*d*), and (*f*) are from Orientation 2. The contact stress is defined as the interaction force between the skeleton and the bilayer per unit area and is shown in units of Pa. In both cases, the snapshots are taken at $t = 0.0145$ s, when the cell has just left the slit. $\delta = 1$ μm. $P = 200$ Pa.

is shown in a micropipette simulation with a two-component DPD algorithm (43).

Another factor that may affect the magnitude of the contact stress is the size of the slit. To illustrate this effect, two additional slit sizes, 0.6 and 1.5 μm, are considered. As shown in Fig. 7 *a*, the transit time T is highly sensitive to slit size δ. Indeed, a reduction of δ from 1.5 to 0.6 μm leads to an increase in T by a factor of 50. The dependence of σ_p upon δ (Fig. 7 *b*), on the other hand, is more complicated. As shown in the figure, decreases in δ may (Orientation 2) or may not (Orientation 1) increase σ_p. This is attributed to the complexity in the deformation mode of the cell membrane as it leaves the slit. As demonstrated in Fig. 8, a smaller slit (e.g., $\delta = 0.6$ μm) generates a narrower tongue on the cell membrane (this is not a tether because it is an intact skeleton-bilayer entity), which may lead to more significant membrane deformation. On the other hand, it also suppresses infolding (as compared with the case when $\delta =$ 1.5 μm) so that less membrane deformation is expected. Consequently the relation between the peak contact stress σ_p (which depends on membrane deformation) and the slit size may not be monotonous. Our results show that compared with the transit time T, σ_p is much less sensitive to δ. For example, as δ decreases from 1.5 to 0.6 μm, T increases from 0.003 to ~0.16 s (for Orientation 1); meanwhile, the variation of σ_p is between −230 and −97 Pa.

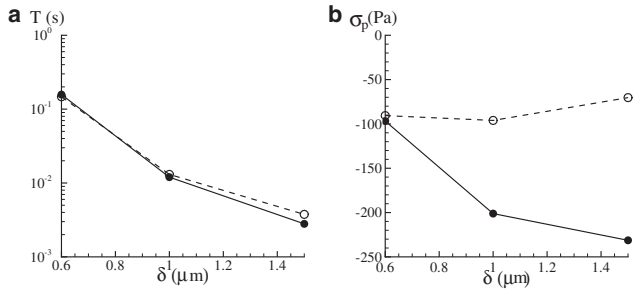

FIGURE 7 Dependencies of the transit time T (*a*) and σ_p (*b*) upon the slit size δ. $P = 200$ Pa. Results from Orientation 1 are shown in solid lines, whereas those from Orientation 2 are shown in dashed lines.

Although the cell deformations in Fig. 8 for Orientations 1 and 2 look similar, there are essential differences between the two. In Orientation 1, the part of the membrane (e.g., the infolded area in Fig. 8 *c*) that experiences the maximum dissociation stress during translocation originates from the dimple region of the cell, whereas in Orientation 2 this part originates from the rim region. As demonstrated in previous studies (e.g., (35)), membrane elements from these two regions maintain their identities during cell deformations and display completely different mechanical characteristics. After the cell recovers its biconcave shape, they will go back to their original locations (i.e., the shape memory effect) (44). Therefore, it is not a surprise that in these two cases there are differences in mechanical response.

To summarize, our simulations suggest that in physiological conditions the possible range of peak dissociation stress between the lipid bilayer and the cytoskeleton is 0.2−0.3 kPa, which is below our previous estimate of 1 kPa. The discrepancy is attributed to the fact that in our previous study the viscosity ratio was chosen to be 1 due to numerical consideration. However, this value is unlikely to happen in vivo. A much more realistic viscosity ratio of 5 is chosen in this study. It greatly diminishes the cell deformation as well as the internal stress.

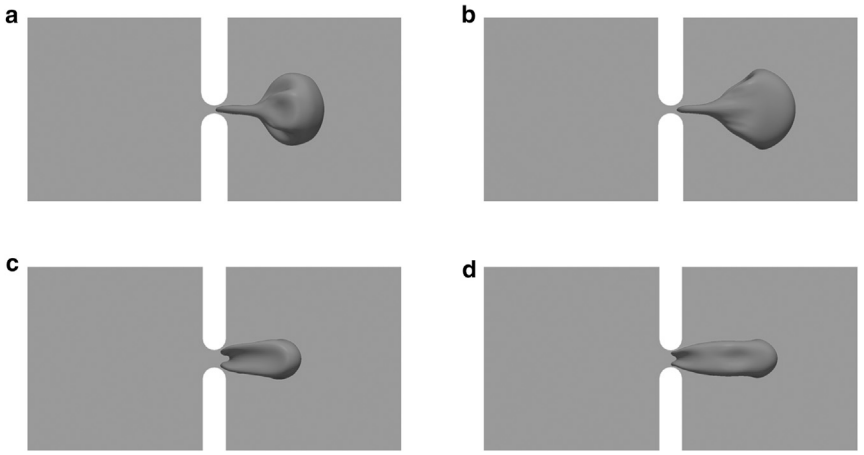

FIGURE 8 Snapshots show cell deformations as the cell leaves the slit with (*a*) $\delta = 0.6$ μm, Orientation 1; (*b*) $\delta = 0.6$ μm, Orientation 2; (*c*) $\delta = 1.5$ μm, Orientation 1; and (*d*) $\delta = 1.5$ μm, Orientation 2. $P = 200$ Pa.

The aging process of RBC is usually accompanied by increase in the viscosity of the cytosol η_2, and subsequently the viscosity ratio Λ. It is interesting that as the cell's viscosity increases, its chances of sequestration, leading to a pathway of removal, increases. For example, we have simulated the translocation of a cell with Orientation 1 at $P = 200$ Pa and $\Lambda = 10$. The transit time changes from 0.012 s (at $\Lambda = 5$) to 0.019 s (at $\Lambda = 10$). This suggests that increase in cell viscosity has a similar effect in transit time as decrease in surface area-to-volume ratio or increase in cell stiffness (28). On the other hand, the peak dissociation stress σ_p changes from -201 to -129 Pa. Thus, as viscosity increases, the intensity of cell deformation decreases, and thereby the probability of vesiculation decreases. This may well suggest that a key role of vesiculation is to preserve erstwhile viable cells against premature removal.

DISCUSSION

The mechanics of separation of the bilipid membrane from the spectrin skeleton has been studied via the formation of tethers extracted from the cell membrane during forced pulling accomplished by either aspiration into pipettes or via pulling attached beads using mechanical or electromechanically induced forces; for example, the work of Waugh and Hochmuth (45), Hochmuth and Marcus (46), Butler et al. (47), Knowles et al. (48), Waugh and Bauserman (49), Hwang and Waugh (50), Borghi and Brochard-Wyart (51), and Waugh et al. (52), has been pivotal in such studies. Fig. 9 illustrates the mechanical scenario whereby a tether is extracted by a force f. It is established that the tether—which, in effect, is a long liquidlike cylinder of lipid membrane—involves the separation of the membrane and spectrin skeleton.

A rough synopsis of the analysis that leads to estimates of the so-called work of separation, γ, and ultimately to estimates of the critical stresses between the membrane and skeleton, would go as follows. The differential free energy, $d\mathcal{F}$, for this under static conditions is given by the incremental work done on the tether extension, as

$$d\mathcal{F} = 2\pi r_t \left(\frac{1}{2}\kappa\frac{1}{r_t^2}\right) dL + 2\pi r_t \Pi\, dL + 2\pi r_t \gamma\, dL. \quad (7)$$

In Eq. 7, the first term represents the differential work of increasing the area of tether that is bent to radius r_t from a nominally flat cell membrane; the bending modulus is κ so that $1/2\kappa/r_t^2$ is bending energy per unit area. The second term comes about as follows: Π is a surface osmotic pressure that arises if the membrane concentrations of integral proteins (e.g., band 3 and glycophorins) are altered and might be thought to be akin to osmotic pressures due to semipermeable membranes separating ionic solutions. Below, we estimate this contribution to $d\mathcal{F}$ as it may matter in the estimate of γ. The analysis of Borghi and Brochard-Wyart (51) describes the dissipative work due to the viscous flow of lipids over the skeleton, which does not concern us here—such work effects are naturally included in our simulations. Noting that the second and third terms both scale with area created, Hochmuth and Marcus (46) define the

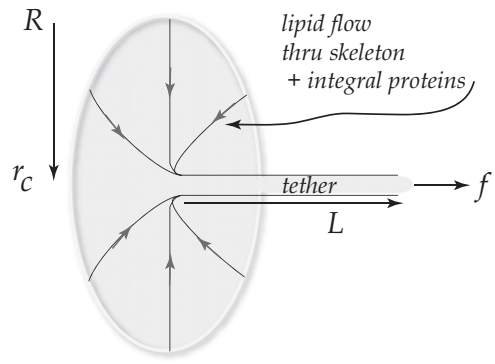

FIGURE 9 Tether formation as forced via aspiration or pulling. The value r_t is the tether's radius and L is its length.

work quantity $\gamma_p = \gamma + \Pi$. It is necessary to explore the osmotic effect at this point.

It has been reported in most tether experiments on presumably healthy cells that integral proteins are deficient in tethers; thus their molar fractions are near 0 rather than the 0.01 they would be in the cell membrane. The lipids are mobile, and we assume equilibrated, from cell membrane to tether and hence a simple balance of their chemical potential would read as

$$\mu^{\circ}_{\ell,c} + RT\ \ln x_{\ell,c} \ = \ \mu^{\circ}_{\ell,t} + RT \ln x_{\ell,t}, \tag{8}$$

where $\mu^{\circ}_{\ell,i}$ is the standard chemical potential for a lipid molecule, ℓ, in the cell membrane or tether, i.e., $i = c,t$, respectively; $x_{\ell,i}$ is the concentration; and RT has the usual meaning. Now we have

$$\mu^{\circ}_{\ell,t} \ = \ \mu^{\circ}_{\ell,c} + \frac{\partial \mu^{\circ}}{\partial p}\delta\, p \ = \ \mu^{\circ}_{\ell,c} + a\delta\, p, \quad \delta\, p \ = \ p_2 - p_1, \tag{9}$$

with a being the partial molar area of a lipid, and $\delta\, p = -\Pi$. The pressure $\delta\, p$ acts so as to inhibit the tether extension and hence, $\delta\, p = -\Pi$. This leads to

$$\delta\, p \ = \ -\Pi \ = \frac{RT}{a}\ln(x_{\ell,c}/x_{\ell,t}). \tag{10}$$

Now, with $R = 8.3(\mathrm{N\cdot m(MK)^{-1}})$, $T \approx 300$ K, and $a \approx 20\ \mathrm{\AA}^2$, we find

$$-\delta\, p \ = \ \Pi \approx 124 \ln(x_{\ell,t}/x_{\ell,c})\ \mathrm{pN}/\mu\mathrm{m} \approx 1.2\ \mathrm{pN}/\mu\mathrm{m} \ \text{ with } \ x_{\ell,c}/x_{\ell,t} \ = \ 0.99. \tag{11}$$

Typical values for γ_t reported are as (46)

$$\gamma_t \approx 74 - 104\ \ \mathrm{pN}/\mu\mathrm{m} \tag{12a}$$

and (50)

$$\gamma_t \approx 59\ \ \mathrm{pN}/\mu\mathrm{m}. \tag{12b}$$

If there is little or no segregation of integral proteins, these estimates should be corrected for the osmotic effect just estimated. This modest correction yields (46)

$$\gamma_t \approx 73 - 103\ \ \mathrm{pN}/\mu\mathrm{m} \tag{13a}$$

and (50)

$$\gamma_t \approx 58\ \ \mathrm{pN}/\mu\mathrm{m}. \tag{13b}$$

It should be noted here, in concern for what follows next, that such tether formation processes do not greatly affect the skeletal density and thus the nominal density of membrane/skeleton anchorages must be broken to achieve separation of membrane from skeleton.

With these numbers we can proceed along two paths to estimate a critical membrane/skeleton stress, $\sigma_{\max}$, for separation.

Path 1

Consider a simple phenomenological cohesive law of the form

$$\sigma \ = \ \zeta\ \delta^{\mathrm{sep}} \mathrm{e}^{-\beta\delta^{\mathrm{sep}}}, \tag{14}$$

where δ^{sep} is the membrane-skeleton separation. Note that $\sigma_{\max} = (\zeta/\beta)e^{-1}$ at $\delta^{\mathrm{sep}}_{\max} = 1/\beta$. With this, γ is computed as

$$\gamma \ = \ \int_0^{\infty} \zeta\delta^{\mathrm{sep}} e^{-\beta\delta^{\mathrm{sep}}} \mathrm{d}\delta^{\mathrm{sep}} \ = \ \zeta \int_0^{\infty} \delta^{\mathrm{sep}} e^{-\beta\delta^{\mathrm{sep}}} \mathrm{d}\delta^{\mathrm{sep}} \ = \ \zeta/\beta^2. \tag{15}$$

Thus we find, with $\gamma = 58$–103 pN/μm,

$$\sigma_{\max} \ = \ \zeta/\beta e^{-1} \ = \ \frac{\beta \ \times \ (87 - 128)}{e}\mathrm{pN}/\mu\mathrm{m}^2. \tag{16}$$

Note that the units of β are m^{-1}. Let $\delta^{\mathrm{sep}}_{\max} = 1$ nm; then $\beta = 10^3\ \mu\mathrm{m}^{-1}$. Then

$$\sigma_{\max} \sim 32 - 58\ \times\ 1000\ \ \mathrm{pN}/\mu\mathrm{m}^2 \sim 32 - 58\ \ \mathrm{kPa}. \tag{17}$$

To put this into another perspective, we note that Peng et al. (18) define the force per junctional complex, $f_{jc} = \sigma A_{jc}$, with A_{jc} being the area per junctional complex and σ being the local stress between the membrane and skeleton. As the nominal areal density of JCs is $\sim\rho^{\circ}_{jc} \approx 275\ \mu\mathrm{m}^{-2}$, the above estimates for $\sigma_{\max}$ would lead to

$$f^{\max}_{jc} \sim 108 - 193\ \ \mathrm{pN}. \tag{18}$$

If $\delta^{\mathrm{sep}}_{\max}$ is larger, say even as large as $\delta^{\mathrm{sep}}_{\max} = 3$ nm, $\sigma_{\max} = 10.8$–19.3 kPa. This would place $f^{\max}_{jc}$ as ~35–62 pN.

The perspective leading to the definition of f_{jc} is that during complex deformations, and depending on the properties of the spectrin skeleton, the areal density of jc values becomes highly variable as discussed below. This can have significant consequences for the prediction of, say $\sigma_{\max} = f^{\max}_{jc}/A_{jc}$. For example, in their simulations of aspiration of an RBC into a pipette of radius 0.668 μm, Peng et al. (18) found that the areal density of jc values can fall to $\rho_{jc} \sim 0.1\ \rho^{\circ}_{jc}$ or less. This would set $\sigma_{\max} \sim$ 500–1000 Pa!. In fact, they reported maximum stresses tending to separate the membrane from the skeleton of order 100–130 Pa and simulated vesiculation. Such large reductions in skeletal density require, however, spectrin unfolding which, in turn, requires that the parameter $F_{1/2}$ be of order $F_{1/2} \sim 7.5$ pN.

Path 2

As analyzed by Evans (53), the most probable breaking force, ϕ, for molecular bonds of the type we are concerned with, is given by

$$\phi(\dot{r}) = \frac{kT}{\delta^{\text{sep}}_{\text{max}}} \ln(\dot{r}/V_1), \quad V_1 = V_0\, e^{-B/kT}, \tag{19}$$

where B is an activation energy $B \approx 20$ kT; $\dot{r}$ is a rate as defined, for example, in connection with Fig. 9, say $\dot{r} \sim 2\ \mu$m/s; $V_0 \sim 10$ m/s is a typical thermal velocity; and we have $kT = 4 \times 10^{-3}$ pN$\cdot\mu$m. Here as before, $\delta^{\text{sep}}_{\text{max}}$ is the critical stretching distance for bond breakage. Evans (53) would assume $\delta^{\text{sep}}_{\text{max}} \sim 1$ nm.

If $\delta^{\text{sep}}_{\text{max}} \sim 1$ nm, for example (as Evans would estimate), we would get

$$\phi(\dot{r} = 2\ \mu\text{m/s}) = 18.4\ \text{pN!} \tag{20}$$

This is an interesting value because it is right in the range (actually at the low end of the range) of most probable unfolding forces for spectrin as analyzed by Zhu and Asaro (32). This might well suggest that it is somewhat improbable to generate such high forces. On the other hand, this value is indeed comparable to the $f^{\text{max}}_{jc} \sim$16–32 pN estimated above. To obtain a critical stress, let us multiply by the areal density, ν, of such bonds (i.e., anchorages) as $\nu \approx 500\ \mu\text{m}^{-2}$ (51). This value for ν now takes into account both band 3 and glycophorin anchorages, whereas in the above only the JC anchorages, with density $\sim\mathring{\rho}_{jc} \approx 275\ \mu\text{m}^{-2}$, were accounted for. This gives, again with $\delta^{\text{sep}}_{\text{max}} \sim 1$ nm,

$$\sigma_{\text{max}} \sim 10\ \text{kPa}, \tag{21}$$

which can be compared to our phenomenological value range of $\sigma_{\text{max}} \sim$ 22–45 kPa. Here again to get to values as low as, say, $\sigma_{\text{max}} \sim 2$ kPa, would require $\delta^{\text{sep}}_{\text{max}} \sim 5$ nm, which would be judged too large.

A dilemma

In summary, it would appear that these estimates of the work of separation and/or the magnitude of critical molecular breaking forces would lead to critical separation stresses in the range $\sigma_{\text{max}} \sim$ 10–30 kPa if $\delta^{\text{sep}}_{\text{max}} \sim 1$ nm. If values of $\delta^{\text{sep}}_{\text{max}} \sim 3$ nm can be justified, then $\sigma_{\text{max}} \sim$ 5–10 kPa may be estimated. As it happens, however, our simulations show that the maximum separation stresses during flow through splenic slits are at most $\sigma_{\text{max}} \lesssim 1$ kPa!. Thus it would appear that, indeed, large reductions in skeletal density are down to the range where $\rho_{jc} \leq 0.1\ \mathring{\rho}_{jc}$ are required to arrive at conditions in which the maximum stresses are sufficient to induce vesiculation. Such reductions in skeletal density can occur in circumstances such as aspiration into narrow pipettes (18), but do not occur in others such as during flow through the splenic sinus slits.

Possible resolution of dilemma

It is believed that with aging, erythrocytes lose hemoglobin via the shedding of vesicles during flow through the spleen (e.g., (10,11,14,15)). It is also believed that as part of this process, hemoglobin binds to band 3 and this "disturbs the anchorage of the lipid bilayer to the cytoskeleton" (11). Indeed, it has been reported that spleen-related vesicles are deficient in skeletal spectrin and related proteins but contain band 3, glycophorin (also an skeletal/membrane anchor), and the shed hemoglobin (10,11,14,15). It is also expected that hemoglobin binding to the membrane will induce local curvature at the binding site, most especially if there is clustering of bound hemoglobins; a scenario is depicted in Fig. 10. Here we illustrate this with respect to the band 3-spectrin binding complex and later we expand the scope of the effects of Hb binding to the JC itself. Indeed, Reynwar et al. (54) have demonstrated via MD simulation that membrane binding of spherical caplike particles can induce high curvatures that can lead to membrane buckling and vesiculation. In addition, Li and Lykotrafitis (55) have also shown, using a coarse-grained MDs model, that spontaneous, or induced, membrane curvatures can develop into small vesicles, i.e., those on the order of the spectrin coral dimensions; these are called "nanovesicles" and may form outside the spleen (also see (56)) during, for example, blood storage. No specific consideration was given here to release of the spectrin network in these studies. Splenic vesicles are found to be, however, somewhat nearly a factor of 10 larger (11); these are referred to as "microvesicles" in the size range of 25–250 nm in diameter.

Taken together, these observations suggest a mechanism of significant reduction of the local skeleton density, or more precisely anchorage density, as is suggested is required for vesiculation. Moreover, binding of hemoglobin, especially in clusters, will likely lead to a high membrane curvature that assists in driving vesiculation during splenic flow. The clustering of hemoglobin into microdomains within the membrane results in, and acts to stabilize, membrane-bending forces and interactions between constituent molecules. The likelihood of changes in

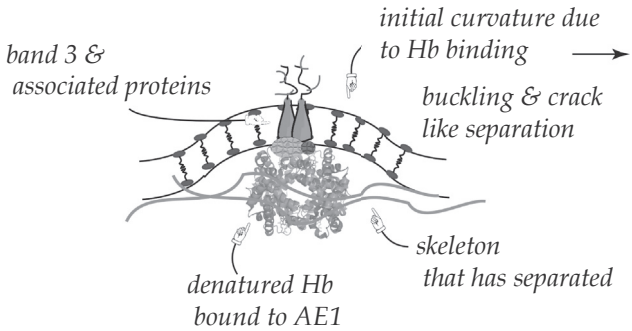

FIGURE 10 Binding of denatured hemoglobin to band 3 causes disturbance of the skeletal/membrane anchor and local curvature.

membrane curvature being the driving force behind erythrocyte vesiculation is soaring, as the binding of hemoglobin to the membrane basal surface not only changes the local membrane interactional and conformational energy of the system, but also inserts amphipathic moieties into the lipid matrix. In the latter case, hemoglobin clusters act as a wedge for the cytoskeleton contractile forces, creating a structural asymmetry and subsequently membrane bending. Furthermore, hemoglobin binding to the membrane affects the lipid composition and asymmetry that exists in the erythrocyte membrane. Lipids in erythrocyte membrane are asymmetrically distributed across the bilayer; the amine-containing phospholipids are enriched on the cytoplasmic surface, whereas the choline-containing lipids and sphingolipids are enriched on the outer surface. The maintenance of transbilayer lipid asymmetry is essential for normal membrane function. In erythrocytes, the asymmetry is generated and maintained by a family of membrane-bound transport proteins called "phospholipid translocases". The best-known translocase is the aminophospholipid flippase, which pumps phosphatidylserine to the membrane inner monolayer (57). Exposure of phosphatidylserine is not always followed by the release of microvesicles, which may be regulated by intracellular calcium (58) and mechanical forces.

CONCLUSIONS

Membrane microvesiculation is an important part of the RBC aging process in vivo, as has been discussed. On the one hand, it contributes to irreversible membrane and hemoglobin loss; this, in turn, leads to an increase in HB concentration and viscosity. Increases in viscosity will eventually result in a reduced ability of the cell to transit venous slits before being eliminated (11). Indeed, although using a nonmolecular based continuum model, it has been shown that the transit times, T, scale as $T \sim \nu_s^{0.5}$; in this study, intra-to-extracellular viscosity ratios of up to 10 were considered (26). Here we find a similar trend, but with $T \sim \nu_s^{0.6}$. Moreover, the membrane loss associated with vesiculation may also shift the cell area-to-volume ratio downward, which has been proposed to mediate the passage or blockage through the venous slits (28).

On the other hand, vesiculation can also be interpreted as a mechanism to remove damaged and signaling-effective components from the cell (59). The exocytosis of nonfunctional proteins through vesiculation not only protects the RBCs from premature death, but also indicates that the same recognition signals mediate the rapid removal of old RBCs and vesicles from circulation (2). Through the continuous release of vesicles, RBCs' indices change as they age, accompanied by progressive increase in cell density and decrease in membrane flexibility. Later we add the observation that as the cytosol viscosity increases the tendency for microvesiculation decreases. This adds additional perspective to the points made just above.

Using our multiscale numerical model, we simulated the dynamic process of RBCs being squeezed through venous slits of the spleen, one of the most extreme loading scenarios in physiological conditions. By simulating the lipids and the cytoskeleton as separate but connected layers, our model was capable of predicting the contact stress between these two, an important parameter associated with the mechanically induced separation of the skeleton from the bilayer and the subsequent formation of vesicles. The model also includes the diffusive motion of the skeleton through the lipid bilayer, and thus describes the changes in skeletal density, and hence anchorage, that occurs during deformation. Our results suggest that the level of dissociation stress that can be achieved in vivo is an order-of-magnitude lower than the critical value for dissociation. This estimate is based on the cell possessing an intact anchorage of skeleton to membrane.

The implication is that for skeleton-bilayer separation to occur in vivo during splenic flow, significant decreases in the density of the anchorage between the cytoskeleton and the lipids is necessary. In ex vivo experiments such as micropipette aspirations, this is achieved by the local area expansion of the cytoskeleton because it is capable of sliding within the lipid bilayer (18). Inside the spleen, however, there is not sufficient time for significant area deformation of the skeleton to occur because the typical transit time is only in the order of 0.1 s (see Fig. 6). We thus conclude that additional mechanisms, e.g., weakening of the skeleton-bilayer connectivity due to the binding of hemoglobin to band 3, must be involved in the in vivo vesiculation of erythrocytes.

This view is consistent with observations of microvesicles extracted from stored blood that contain ankyrin (bound to glycophorin) and band 3 in aggregated and degraded forms (22). It is also consistent with observations of increased microvesiculation in cases of hereditary anemias (19). In these cases, either the skeleton is disrupted or in the case of hemoglobinopathies, altered hemoglobin may bind to anchor proteins and disrupt anchorage. Therefore, although it seems clear that RBC vesiculation is indeed promoted by flow through the venous slits of the spleen, it appears that biochemical factors associated with aging and/or with pathology play a definite role in regulating the process. Thus, additional attention is required to provide a more comprehensive analysis of vesiculation, including effects of biochemical changes to the integral and cytoskeleton proteins. Phenomena such as aggregation of degraded proteins and their binding to the membrane, thus causing large curvatures, need to be explored as part of this, to our knowledge, new comprehensive analysis (54).

Our findings also support, to our knowledge, a new paradigm for splenic vesiculation that would go like this: during cell aging, the binding of denatured hemoglobin to band 3, and hence to the JC complex (see Figs. 10 and 11), causes a

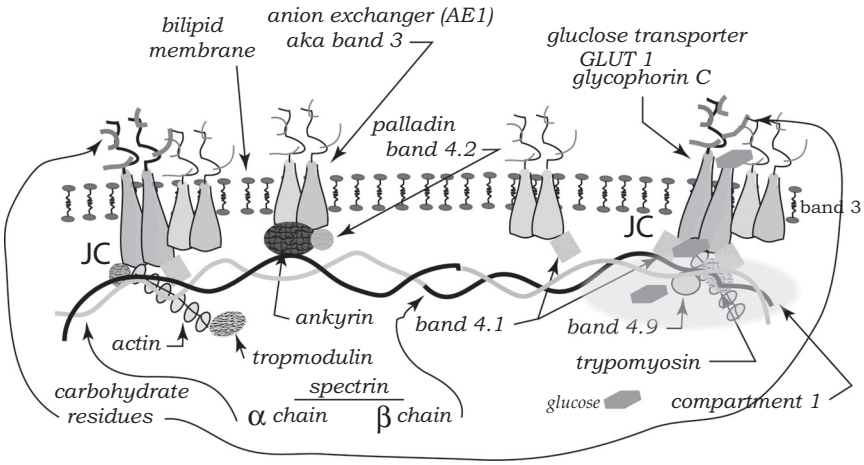

FIGURE 11 Detailed molecular makeup of the band 3-spectrin and JC-spectrin complexes (19,60–62). Binding of denatured hemoglobin to band 3 and the JC causes disturbance of the skeletal/membrane anchor and local curvature.

reduction in the density of skeleton-to-membrane connection. Fig. 11 illustrates that not only the band-3 link is vulnerable as shown in Fig. 10 but the JC complex itself may be disrupted as well (also see (19,60–62)). This then allows for microvesiculation that leads to a reduction in membrane area, cell volume, and hemoglobin content, but to an increase in hemoglobin concentration. The increase in viscosity due to increased hemoglobin concentration and the reduction in membrane area leads to increased transit times and possible cell blockage, both promoting cell removal. Yet higher cytosol viscosities tend to suppress continued microvesiculation and hence cells are unlikely to be prematurely removed.

ACKNOWLEDGMENTS

The authors thank Dr. Zhangli Peng at the University of Notre Dame for assistance in method development.

REFERENCES

1. Mebius, R., and G. Kraal. 2005. Structure and function of the spleen. *Nat. Rev. Immunol.* 5:606–616.
2. Willekens, F. L. A., J. M. Weere, …, G. J. C. G. M. Bosman. 2008. Erythrocyte vesiculation: a self-protective mechanism? *Br. J. Haematol.* 141:549–556.
3. Winslow, R. M., and W. F. Anderson. 1978. The hemoglobinopathies. *In* The Metabolic Basis of Inherited Disease. J. B. Stanbury, J. B. Wyngaarden, and D. S. Fredricks, editors. McGraw-Hill, New York, NY, pp. 1465–1507.
4. Weatherall, D. J., J. B. Clegg, …, W. G. Wood. 1995. The hemoglobinopathies. *In* The Metabolic and Molecular Basis of Inherited Disease, *Vol. III*. C. R. Scriver, A. L. Beaudet, S. S. William, and D. Valle, editors.. McGraw-Hill, New York, NY, pp. 3413–3484.
5. Jacob, H. S. 1970. Mechanisms of Heinz body formation and attachment red cell membrane. *Semin. Hematol.* 7:341–353.
6. Bratosin, D., J. Mazurier, …, J. Montreuil. 1998. Cellular and molecular mechanisms of senescent erythrocyte phagocytosis by macrophages, a review. *Biochimie.* 80:173–195.
7. MacDonald, I. C., D. M. Ragan, …, A. C. Groom. 1987. Kinetics of red blood cell passage through interendothelial slits into venous sinuses in rat spleen, analyzed by in vivo microscopy. *Microvasc. Res.* 33: 118–134.
8. Chen, L. T., and L. Weiss. 1973. The role of the sinus wall in the passage of erythrocytes through the spleen. *Blood.* 41:529–537.
9. Delplaine, G., …, P. A. Buffet. 2011. The sensing of poorly deformable red blood cells by the human spleen can be mimicked in vitro. *Blood.* 117:e88–e95.
10. Willekens, F. L. A., B. Bregt-Roerdinkholder, …, J. M. Weere. 2003. Haemoglobin loss from erythrocytes in vivo results from spleen-facilitated vesiculation. *Blood.* 101:747–751.
11. Bosman, G., F. L. A. Willekens, and J. M. Weere. 2012. Erythrocyte senescence. *In* Erythrocytes, Physiology and Pathophysiology. F. Land and M. Föller, editors. Imperial College Press, London, United Kingdom.
12. Iglič, A., S. Svetina, and B. Žekš. 1995. Depletion of membrane skeleton in red blood cell vesicles. *Biophys. J.* 69:274–279.
13. Yu, J., and D. Branton. 1976. Reconstitution of intramembrane particles in recombinants of erythrocyte band 3 and lipid: effects of spectrin-actin association. *Proc. Natl. Acad. Sci. USA.* 11:3891–3895.
14. Dumaswala, U. J., and T. J. Greenwalt. 1984. Human erythrocytes shed exotic vesicles in vivo. *Transfusion.* 24:490–492.
15. Synder, L. M., G. Fairbanks, …, L. Leb. 1985. Properties and characterization of vesicles released by young and old human red cells. *Br. J. Haematol.* 59:513–522.
16. Williams, A. R., and D. R. Morris. 1980. The internal viscosity of the human erythrocyte may determine its lifespan in vivo. *Scand. J. Haematol.* 24:57–62.
17. Usami, S., S. Chen, and M. I. Gregersen. 1970. Viscometric behavior of young and aged erythrocytes. *In* Theoretical and Clinical Hemorheology. H. H. Hartert and A. L. Copely, editors. Pergamon Press, Oxford, United Kingdom, pp. 266–270.
18. Peng, Z., R. J. Asaro, and Q. Zhu. 2010. Multiscale simulation of erythrocyte membrane. *Phys. Rev. E Stat. Nonlin. Soft Matter Phys.* 81: 031904.
19. Alaarg, A., R. M. Schillelers, …, R. van Wijk. 2013. Red blood cell vesiculation in hereditary hemolytic anemia. *Front. Physiol.* 365:1–15.
20. Mullier, E., N. Bailly, …, J. Dognè. 2012. Quantification and characterization of microvesicles: applications in hereditary spherocytosis, type II heparin-induced thrombocytopenia and cancer. *Belg. J. Hematol.* 3:157–160.
21. Mokken, F. C., M. Kedaria, …, A. W. Gelb. 1992. The clinical importance of erythrocyte deformability, a hemorheological parameter. *Ann. Hematol.* 64:113–122.

22. Kriebarbis, A. G., M. H. Antonelou, and K. E. Stamoulis. 2008. RBC-derived vesicles during storage: ultrastructure, protein composition, oxidation, and signaling components. *Transfusion.* 48:1943–1953.
23. Bosman, G. J., E. Lasonder, and M. Luten. 2008. The proteome of red cell membranes and vesicles during storage in blood bank conditions. *Transfusion.* 48:827–835.
24. Greenwalt, T. J. 2006. The how and why of exocytic vesicles. *Transfusion.* 46:143–152.
25. Salzer, U., R. Zhu, and M. Luten. 2008. Vesicles generated during storage of red cells are rich in the lipid raft marker stomatin. *Transfusion.* 48:451–562.
26. Freund, J. 2013. The flow of red blood cells through a narrow spleen-like slit. *Phys. Fluids.* 25:110807.
27. Salehyar, S., and Q. Zhu. 2016. Deformation and internal stress in a red blood cell as it is driven through a slit by an incoming flow. *Soft Matter.* 12:3156–3164.
28. Pivkin, I. V., Z. Peng, …, S. Suresh. 2016. Biomechanics of red blood cells in human spleen and consequences for physiology and disease. *Proc. Natl. Acad. Sci. USA.* 113:7804–7809.
29. Chien, S. 1987. Red cell deformability and its relevance to blood flow. *Annu. Rev. Physiol.* 49:177–192.
30. Kesmarky, G., P. Kenyeres, …, K. Toth. 2008. Plasma viscosity: a forgotten variable. *Clin. Hemorheol. Microcirc.* 39:243–246.
31. Pozrikidis, C. 2005. Axisymmetric motion of a file of red blood cells through capillaries. *Phys. Fluids.* 17:031503.
32. Zhu, Q., and R. Asaro. 2008. Spectrin folding vs. unfolding reactions and RBC membrane stiffness. *Biophys. J.* 94:2529–2545.
33. Zhu, Q., C. Vera, …, L. A. Sung. 2007. A hybrid model for erythrocyte membrane: a single unit of protein network coupled with lipid bilayer. *Biophys. J.* 93:386–400.
34. Peng, Z., R. Asaro, and Q. Zhu. 2011. Multiscale modelling of erythrocytes in Stokes flow. *J. Fluid Mech.* 686:299–337.
35. Peng, Z., and Q. Zhu. 2013. Deformation of the erythrocyte cytoskeleton in tank treading motions. *Soft Matter.* 9:7617–7627.
36. Alberts, B., A. Johnson, …, P. Walter. 2002. The Cell. Garland Science, New York, NY.
37. Weinbaum, S., J. M. Tarbell, and E. R. Damiano. 2007. The structure and function of the endothelial glycocalyx. *Annu. Rev. Biomed. Eng.* 9:121–167.
38. Neu, B., S. O. Sowemimo-Coker, and H. J. Meiselman. 2003. Cell-cell affinity of senescent human erythrocytes. *Biophys. J.* 85:75–84.
39. Rasia, M., and A. Bollini. 1998. Red blood cell shape as a function of medium's ionic strength and pH. *Biochim. Biophys. Acta.* 1372: 198–204.
40. Fernandes, H. P., C. L. Cesar, and M. de Lourdes Barjas-Castro. 2011. Electrical properties of the red blood cell membrane and immunohematological investigation. *Rev. Bras. Hematol. Hemoter.* 33:297–301.
41. Masliyah, J., and S. Bhattacharjee. 2006. Electrokinetic and Colloid Transport Phenomena. John Wiley & Sons, Hoboken, NJ.
42. Mohandas, N. E., and E. Evans. 1994. Mechanical properties of the red cell membrane in relation to molecular structure and genetic defects. *Annu. Rev. Biophys. Biomol. Struct.* 23:787–818.
43. Peng, Z., X. Li, …, S. Suresh. 2013. Lipid bilayer and cytoskeletal interactions in a red blood cell. *Proc. Natl. Acad. Sci. USA.* 110:13356–13361.
44. Fischer, T. M. 2004. Shape memory of human red blood cells. *Biophys. J.* 86:3304–3313.
45. Waugh, R. E., and R. M. Hochmuth. 1987. Mechanical equilibrium of thick, hollow, liquid membrane cylinders. *Biophys. J.* 52:391–400.
46. Hochmuth, R. M., and D. Marcus. 2002. Membrane tethers formed from blood cells with available area and determination of the adhesion energy. *Biophys. J.* 82:2964–2969.
47. Butler, J., N. Mohandas, and R. E. Waugh. 2008. Integral protein linkage and the bilayer-skeleton separation energy in red blood cells. *Biophys. J.* 95:1826–1836.
48. Knowles, D. W., L. Tilley, …, J. A. Chasis. 1997. Erythrocyte membrane vesiculation: model for the molecular mechanism of protein sorting. *Proc. Natl. Acad. Sci. USA.* 94:12969–12974.
49. Waugh, R. E., and R. G. Bauserman. 1995. Physical measurements of bilayer-skeletal separation forces. *Ann. Biomed. Eng.* 23:308–321.
50. Hwang, W. C., and R. E. Waugh. 1997. Energy of dissociation of lipid bilayer from the membrane skeleton of red blood cells. *Biophys. J.* 72:2669678.
51. Borghi, N., and F. Brochard-Wyart. 2007. Tether extrusion from red blood cells: integral proteins unbinding from cytoskeleton. *Biophys. J.* 93:1369–1379.
52. Waugh, R. E., A. Mantalaris, …, J. H. Wu. 2001. Membrane instability in late-stage erythropoiesis. *Blood.* 97:1869–1875.
53. Evans, E. 2001. Probing the relation between force-lifetime and chemistry in single molecular bonds. *Annu. Rev. Biophys. Biomed. Struct.* 30:105–128.
54. Reynwar, B. J., G. Illya, …, M. Deserno. 2007. Aggregation and vesiculation of membrane proteins by curvature-mediated interactions. *Nature.* 447:461–464.
55. Li, H., and G. Lykotrafitis. 2015. Vesiculation of healthy and defective red blood cells. *Phys. Rev. E Stat. Nonlin. Soft Matter Phys.* 92:012715.
56. Sens, P., and N. Gov. 2007. Force balance and membrane shedding at the red-blood-cell surface. *Phys. Rev. Lett.* 98:018102.
57. Daleke, D. L. 2003. Regulation of transbilayer plasma membrane phospholipid asymmetry. *J. Lipid Res.* 44:233–242.
58. Boulanger, C. M., N. Amabile, and A. Tedgui. 2006. Circulating microparticles: a potential prognostic marker for atherosclerotic vascular disease. *Hypertension.* 48:180–186.
59. Kriebardis, A., M. Antonelou, …, P. Issidora. 2012. Cell-derived microparticles in stored blood products: innocent-by-standers or effective mediators of post-transfusion reactions? *Blood Transfus.* 10 (*Suppl 2*):s25–s38.
60. Mohandas, N., and P. G. Gallagher. 2008. Red cell membrane. *Blood.* 112:161136.
61. Lux, S. E. 2015. Anatomy of the red blood cell membrane skeleton: unanswered questions. *Blood.* 127:187–199.
62. Khan, A. A., T. Hanada, …, A. H. Chishti. 2008. Dematin and adducin provide a novel link between the spectrin cytoskeleton and human erythrocyte membrane by directly interacting with glucose transporter-1. *J. Biol. Chem.* 283:14600–14609.
63. Otter, W. K., and S. A. Shkulipa. 2007. Intermonolayer friction and surface shear viscosity of lipid bilayer membranes. *Biophys. J.* 93:423–433.
64. Tran-Son-Tay, R., S. Sutera, and P. Rao. 1984. Determination of red blood cell membrane viscosity from rheoscopic observations of tank-treading motion. *Biophys. J.* 46:65–72.
65. Evans, E., and R. Skalak. 1980. Mechanics and Thermodynamics of Biomembranes. CRC Press, Boca Raton, FL.